frontiers | Frontiers in Nanotechnology

TYPE Original Research
PUBLISHED 29 July 2024
DOI 10.3389/fnano.2024.1392694

OPEN ACCESS

EDITED BY
Ashok Kumar Nadda,
Jaypee University of Information Technology, India

REVIEWED BY
Supriya Atta,
Duke University, United States
Iram Maqsood,
University of Maryland, United States

*CORRESPONDENCE
Marcelo Y. Icimoto,
icimoto@unifesp.br
Iseli L. Nantes,
ilnantes@gmail.com,
ilnantes@ufabc.edu.br

†These authors have contributed equally to this work

RECEIVED 27 February 2024
ACCEPTED 09 July 2024
PUBLISHED 29 July 2024

CITATION
Batista CCS, Toledo VH, Ramos MPC, Oliveira V, Acuña J, Icimoto MY and Nantes IL (2024), Effect of chiral silver nanoparticles on prolyl-oligopeptidase binding and activity. *Front. Nanotechnol.* 6:1392694. doi: 10.3389/fnano.2024.1392694

Effect of chiral silver nanoparticles on prolyl-oligopeptidase binding and activity

Carin C. S. Batista[1†], Victor H. Toledo[1†], Marcos P. C. Ramos[2], Vitor Oliveira[2], Javier Acuña[1], Marcelo Y. Icimoto[2*] and Iseli L. Nantes[1*]

[1]Laboratory of Nanostructures for Biology and Advanced Materials, Center of Biological Sciences and Humanities, Federal University of ABC, Santo André, Brazil, [2]Biophysical Department, Escola Paulista de Medicina (EPM), Federal University of São Paulo (UNIFESP), São Paulo, Brazil

Introduction: Silver nanoparticles have a diversity of applications both in biological and technological areas. More recently, studies conducted in the Nano/Bio interface have demonstrated that chiral nanocrystals grew in chiral templates, and nanostructures functionalized with chiral molecules present specific properties. These properties apply to advanced materials, energy, medicine, and pharmacology.

Methodology: The present study synthesized silver nanoparticles on silver seeds using D- and L-histidine as templates and borohydride as a reducing agent.

Results and Discussion: The nanoparticles were characterized by UV-visible spectroscopy and presented surface plasmon resonance (SPR) bands around 415 nm. CD spectra showed signals in the region of the SPR band, indicating the growth of nanocrystals with chiral distortion. Synthesized silver nanoparticles were also characterized by high-resolution transmission electron microscopy (HRTEM), which evidenced the presence of histidine corona. The silver nanoparticles were functionalized with prolyl-oligopeptidase (POP), a prolinespecific endopeptidase expressed in the brain. This enzyme cleaves neuroactive peptides involved in memory, learning, and neurodegeneration. The enzyme POP was expressed with a His-tag to provide competitive binding affinity to silver nanoparticles covered by D- and L-histidine. Considering the biological importance, POP was chosen as a model for studying the functionalization of chiral silver nanoparticles regarding the chiral discrimination for binding affinity and stabilization.

KEYWORDS

chiral silver nanoparticles, histidine, prolyl-oligopeptidase, binding affinity, circular dichroism, HRTEM

1 Introduction

Chirality is a geometric characteristic presented by molecules, their supramolecular associations, and structures not superimposable with their mirror images. Chiral structures and their respective mirror images constitute pairs called enantiomers or enantiomorphs. (Qiu et al., 2018; Xiao et al., 2020a; Wen et al., 2021). As discussed by Cho et al., 2023,

10.3389/fnano.2024.1392694

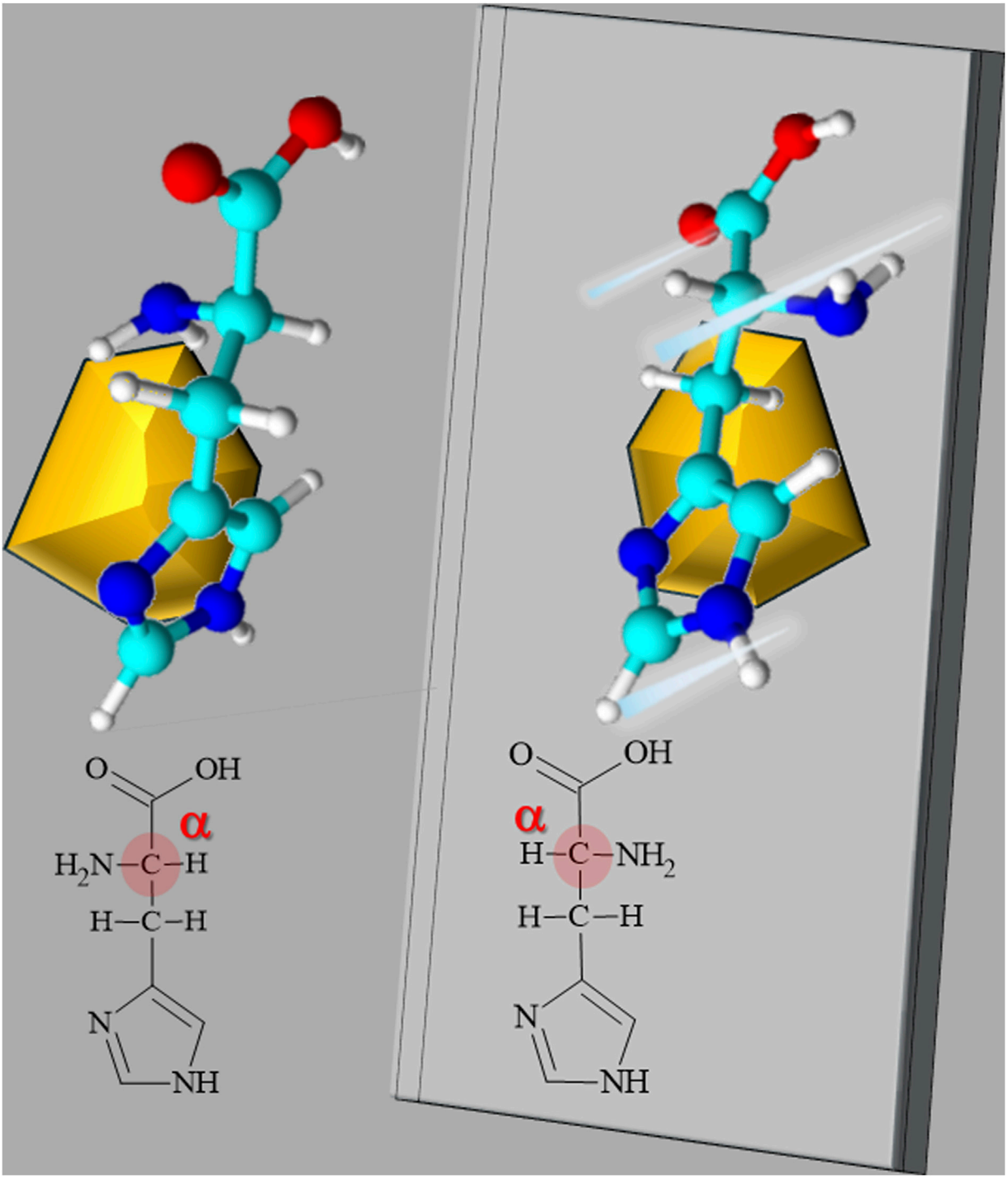

FIGURE 1
Schematic representation of enantiomeric pair of histidine confining a nanocrystal with chiral distortion. The Fisher structure of L- and D-histidine is shown with the chiral center, the α-carbon, highlighted in red. Above, the L- and D-histidine tridimensional structures are shown with a sketch of a nanocrystal grown with chiral distortion templated by the enantiomers. The D-isomers were represented as mirror images.

chirality can also be explained within the framework of group theory, where an object, like a molecule, is considered chiral only if it lacks improper rotation axes (Sn) in its structure.

Chirality is a pervasive characteristic, and living organisms contain many chiral substances. A prime example is the amino acids found in biological cells in their left-handed, L-enantiomeric form, while sugars take on a right-handed, D-enantiomeric configuration (Basak et al., 2017; Zhao et al., 2020). Distinct biological properties are conferred to chiral substances based on their handedness (Oh et al., 2021). In nature, proteins, which are naturally chiral polymers, function as templates for the growth of crystalline structures. A well-

known example is the triple collagen helix that orients the deposition of calcium hydroxyapatite during the calcification of bones and teeth (Oh et al., 2022).

Another example is the iron storage protein ferritin, in which iron ions crystallize as ferrihydrite (Houben et al., 2020). The use of chiral geometry to promote the crystal growth of nanostructures with chiral lattice distortion has been described in the literature in recent years (Yeom et al., 2018; Ghosh et al., 2020). Ghosh et al. produced thin films of chiral cobalt oxide using D and L tartaric acid (Ghosh et al., 2020). Yeom et al. (2018) synthesized chiral cobalt oxide nanoparticles using D and L cysteine. Jiang et al. (2017) reported the synthesis of chiral ceramic nanoparticles of WO3-x.H_2O of 1.6 nm facilitated by using proline and aspartic acid. The ceramic nanoparticles catalyzed the formation of peptide bonds between the amino acids used in the synthesis. Tomato extracts were efficiently used to synthesize nanostructured metal oxides that were templated by the nanocage of the plant protein ferritin. Adding gold salt to tomato pulp extract converts endogenous ferrihydrite to superparamagnetic Fe_3O_4 concomitantly with the formation of gold nanoparticles (Nantes-Cardoso et al., 2019; Tofanello et al., 2021). Also, chiromagnetic Co_3O_4 quantum dots were produced using plant and animal ferritins (Bronzato et al., 2022). The enantiomeric pair of chiral Co_3O_4 nanoparticles was recently obtained using D- and L-histidine as templates. The nanoparticles could be applied to discriminate and quantify isomers of penicillamine (Liu et al., 2023).

Chirality is extended to the field of physics. For instance, electromagnetic waves propagate left- or right-handed (Tang and Cohen, 2011). Consequently, chiral chromophores only absorb circularly polarized light to the left or right, allowing the chirality of substances and structures to be measured using optical devices employing either left-handed (LCP) or right-handed circularly polarized light (RCP) (Mun et al., 2020). The absorption spectra generated by the selective absorption of RCP and LCP are called circular dichroism (CD) (Halas et al., 2011). Also, the spin of an electron reveals chirality to it. Thus, chiral nanostructured materials conduct electrons with spin selectivity (Naaman and Waldeck, 2015). The combination of quantum confinement and catalytic properties of nanocrystals has allowed the evolution of traditional optical devices with the creation of flexible screens and the achievement of selective enantiomeric reactions (Cornelissen et al., 2001; Halas et al., 2011). In nanostructures, chirality can be obtained in individual nanoparticles or chiral arrangements. More recently, materials scientists observed that chirality in nanomaterials confers new physicochemical properties. Chiral inorganic and self-assembled nanostructures have shown immense potential in many fields. Some possible applications of chiral nanostructured materials are devices for circularly polarized light emission, chiral nanomaterial for interaction with biological systems for studying chiral-dependent nanotoxicity and therapeutics, Second-harmonic generation for second-order nonlinear optics as observed for chiral perovskite nanowires, chiral catalysis that is crucial for the food, chemical, and medical industries, production of chiral assemblies, production of chiral nano system-based sensing, potential therapeutics, and vaccines (Naito et al., 2010; Suzuki et al., 2016; Hatano et al., 2018; Malishev et al., 2018; Peng et al., 2018; Yuan et al., 2018; Đorđević et al., 2018; Xiao et al., 2020b; Xu et al., 2022; Gao et al., 2024).

The present study describes the chiral-induced selective binding and activity of prolyl oligopeptidase on silver nanocrystals that were templated by the enantiomeric pair of histidine (Figure 1).

Prolyl-oligopeptidase (POP) belongs to the serine protease family and is crucial in regulating protein synthesis, folding, and degradation to ensure proper cellular function and homeostasis (Polgár, 2002). As protease, POP is involved in the cleavage of peptide bonds at proline residues in short oligopeptides. Furthermore, POP engages in critical interactions with essential partner proteins, shaping its role in cellular processes (Rea and Fulop, 2011). Notably, POP has been demonstrated to interact with Fibroblast Growth Factor 23 (FGF23), influencing phosphate and vitamin D metabolism disorders, including X-linked hypophosphatemia (Prohaska and Salzer, 2018). The involvement of POP in the cleavage of alpha-synuclein (Lambeir, 2011; Santos et al., 2020) beta-amyloid peptides (Hannula et al., 2013), interactions with proteins such as Insulin-Degrading Enzyme (IDE) (Ferro et al., 2020) and huntingtin (Norrbacka et al., 2019) associates this enzyme with neurodegenerative disorders like Parkinson's disease, Alzheimer's disease, and Huntington's disease. Prolyl oligopeptidase is critical in degrading proteins that accumulate in the retinal pigment epithelium cell layer, essential for preventing age-related macular degeneration (AMD). Aging, chronic oxidative stress, and protein accumulation impair the epithelium cell layer, eventually leading to cell death and blindness and causing reading and facial recognition difficulties. The study of models to understand the mechanism of action of prolyl oligopeptidase is crucial to understanding the molecular bases of AMD (Kaarniranta et al., 2013; Kauppinen et al., 2016; Toppila et al., 2023).

The chiral-dependent association of POP with nanostructured material can contribute to mitigating nanotoxicity and developing the therapeutic applications of this enzyme.

2 Materials and methods

2.1 Chemicals

Nitrate ($AgNO_3$), sodium borohydride ($NaBH_4$), cetyltrimethylammonium bromide ($C_{19}H_{42}BrN$), L-Histidine and D-Histidine ($C_6H_9N_3O_2$), all analytical grade, were acquired from Sigma-Aldrich and used as received. The water was pre-treated using the Milli-Q® Plus System (Millipore Corporation).

2.2 Wet route for chemical synthesis of AgNPs templated and stabilized by L- and D-Histidine

Chiral silver nanocrystals were grown on Ag seeds. The Ag seeds were synthesized according to the protocol used by Hyo-Yong Ahn et al. (Ahn et al., 2013). The synthesis is carried out at room temperature and is initiated with a solution of 10 mM $AgNO_3$ and 100 mM CTAB homogenized in 10 mL of water.

A 0.08 mL of 10 mM $NaBH_4$ solution is dripped into the solution containing $AgNO_3$ and CTAB under rapid stirring. The solution turns dark brown and should be left to stand for 24 h so that the borohydride decomposes, and the solution with the seeds is stored

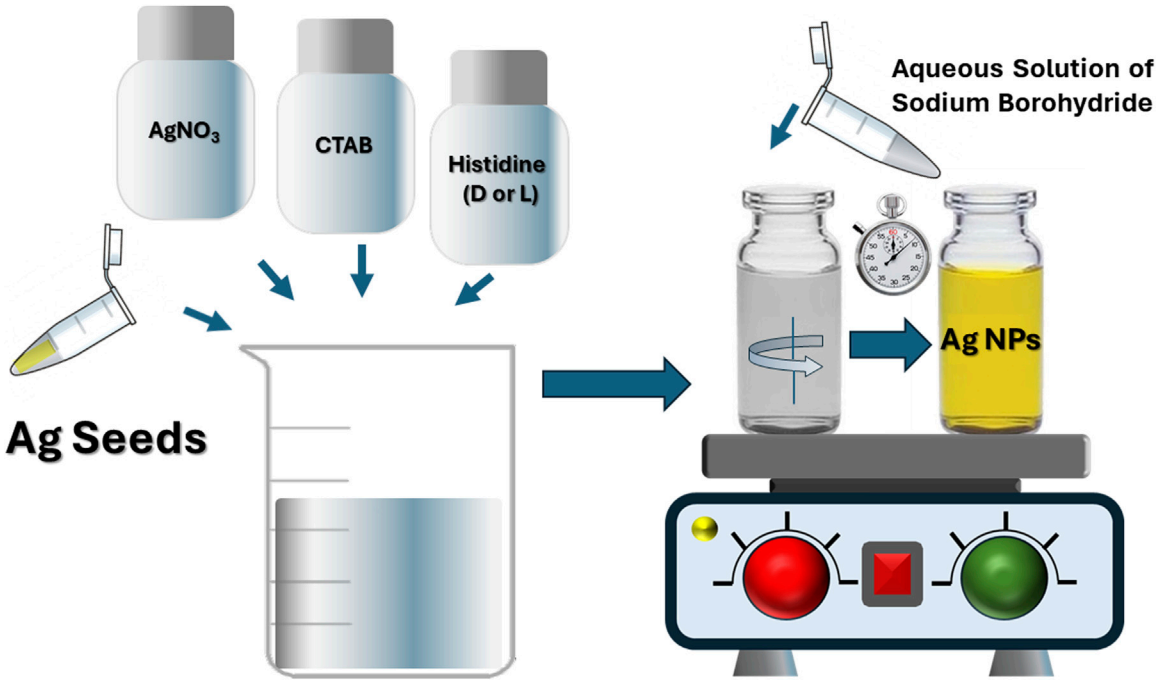

FIGURE 2
Schematic representation of the procedure used in the chemical synthesis of chiral AgNPs by wet route. On the left, the preparation of stock solution is shown, and on the right, the synthesis of chiral AgNPs.

under refrigeration to maintain stability. With the silver seeds ready, the second step is the preparation of AgNPs. The synthesis is carried out by adding dropwise a stock solution containing 10 mM (50 µL) $NaBH_4$ to an aqueous solution containing 10 mM $AgNO_3$ (200 µL), 5 mM CTAB (1.6 mL), 950 µL of L- or D-Histidine at concentrations of 50 mM and100 mM and 5 µL of the Ag seed solution. The solution is prepared at room temperature and remains under stirring for 1 h (Batista et al., 2021), as shown in Figure 2. The AgNPs remained stable for 1 year without significant changes in the SPR bands (Supplementary Figure S1).

2.3 Dynamic light scattering (DLS)

Dynamic Light Scattering (DLS) measurements were performed using the ALV/CGS-3 equipment, which consists of a polarized HeNe laser (22 mW) operating at a wavelength (λ) of 633 nm, a digital correlator ALV 7004, and a pair of APD detectors operating in pseudo-cross-correlation mode. The samples were placed in 10 mm diameter glass cuvettes and maintained at a constant temperature of 25°C ± 1°C. Temporal correlation functions were acquired at an angle of 90° and were adjusted using the Cumulants method.

2.4 Static light scattering (SLS)

Static Light Scattering (SLS) measurements were conducted using the same equipment as in the DLS measurements but in the angular range of 30°–150°. When possible, the radius of gyration (RG) of the AgNPs was obtained using the Zimm equation.

2.5 Electrophoretic light scattering (ELS)

Electrophoretic Light Scattering analyses were carried out using the Zetasizer Nano ZS equipment (Malvern Instruments, United Kingdom). The nanoparticles' zeta potential (ζ) was determined through electrophoretic mobility (UE) measurements, and values were converted using the Henry equation.

2.6 High-resolution transmission electron microscopy (HRTEM)

Samples for image analysis were prepared by evaporating a drop of the samples onto copper supports coated with ultra-thin carbon film. Micrographs were acquired using high-resolution transmission microscopy (HRTEM—Thermo Fischer Talos F200X-G2) operating at 200 kV accelerating voltage using a cold field emission gun (X-FEG). The CrysTBox and Java Electron Microscopy Software (JEMS) were used to treat diffraction images. The obtained data for the sample were then compared with data available in crystallography databases to confirm the composition and phase of the synthesized and analyzed sample. The database used was the "Inorganic Crystal Structure Database - ICSD," from which the CIF file containing the silver crystallographic data was exported (Majee et al., 2020). The same image processing software opens the reference file, which automatically detects diffraction rings,

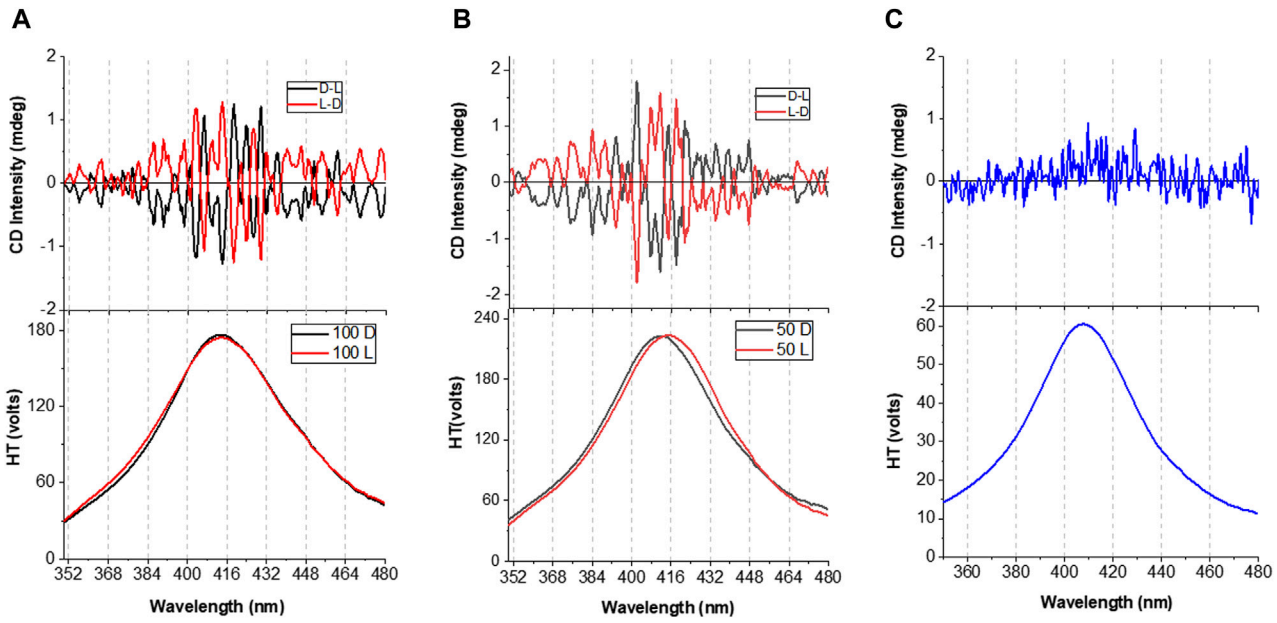

FIGURE 3
UV-visible and CD spectra of chiral AgNPs. **(A)** CD bands (upper panels) and the corresponding SPR (lower panels) of AgNPs synthesized with 100 mM of D- (black lines) and L-(red lines) histidine. **(B)** CD band (uppper panel) and the corresponding SPR (lower panel) of AgNPs synthesized with 50 mM of D- (black lines) and L-(red lines) histidine. The CD spectra result from baseline subtraction and remotion of CD contribution without mirror image pair. The CD of L-AgNPs was subtracted from the signal of D-AgNPs and vice versa, as indicated in each panel. **(C)** CD spectrum and the corresponding SPR band of the Ag seeds. The SPR bands were obtained simultaneously with CD analysis expressed as the tension in the photomultiplier.

indexes planes based on the reference file, and compares interplanar distance values. It is worth noting that, in some cases, the program repeats planes for two different rings due to the proximity of values and the lack of a specific plane assigned to that ring. In such cases, the one that most closely matches the reference value is manually selected.

2.7 UV-visible spectroscopy

UV-visible spectroscopy data were acquired using a Thermo Scientific Evolution 201 spectrometer. The wavelength scanning resolution was 1.0 nm. Measurements were performed using a quartz cell with an optical path of 1.0 cm.

2.8 Circular dichroism (CD)

Circularly polarized light spectroscopy data were obtained using a Jasco J-815 spectropolarimeter (circular dichroism). The wavelength range scanned was from 800 to 250 nm, and for each sample, 11 runs were performed using a quartz cell with an optical path of 1.0 cm.

2.9 Expression and characterization of recombinant human POP

Recombinant POP was expressed using the pET-28a vector in *E. coli* and purified through Ni-NTA affinity chromatography (Neves et al., 2023). Purity and identity were confirmed via SDS-PAGE. Activity is measured using the Tris-HCl buffer (pH 7.4) for optimal activity. Z-gly-pro-MCA (Sigma Aldrich) substrate was dissolved in DMSO to create a 10 mM stock solution, further diluted to 100 μM in the enzyme reaction buffer for experimentation. A 96-well plate was prepared with controls and blanks, combining recombinant POP and substrate in each well under consistent reaction conditions. A Shimadzu F7000 Plate Fluorometer was employed with excitation and emission wavelengths set at 380 and 460 nm, respectively (Icimoto et al., 2020; Brito et al., 2021). Fluorescence was measured at intervals to monitor the enzymatic reaction and sample comparison. Data was analyzed using Grafit 5.0 (Erithacus software) (Gontijo et al., 2021).

3 Results and discussions

The silver nanoparticles were synthesized using D- and L-histidine as templates and characterized by different techniques. An important issue was the synthesis of silver nanocrystals with chiral distortion that was corroborated by CD spectroscopy. Figures 2A–D) show that CD signals were obtained in the wavelength region of the AgNP surface plasmon resonance (SPR) bands. The CD spectra for AgNPs synthesized 50 and 100 mM of D- and L-histidine showed perfect mirror symmetry with chiroptical contributions (Figures 3A, B). The contributions of AgNP populations that are not enantiomeric pairs and reminiscent seeds were excluded by the subtraction of the signal of L AgNPs from D AgNPs and *vice versa*. Figure 3C) shows the low-intensity and noised signal obtained with achiral seeds. The SPR bands were obtained simultaneously with CD analysis, and the intensity is

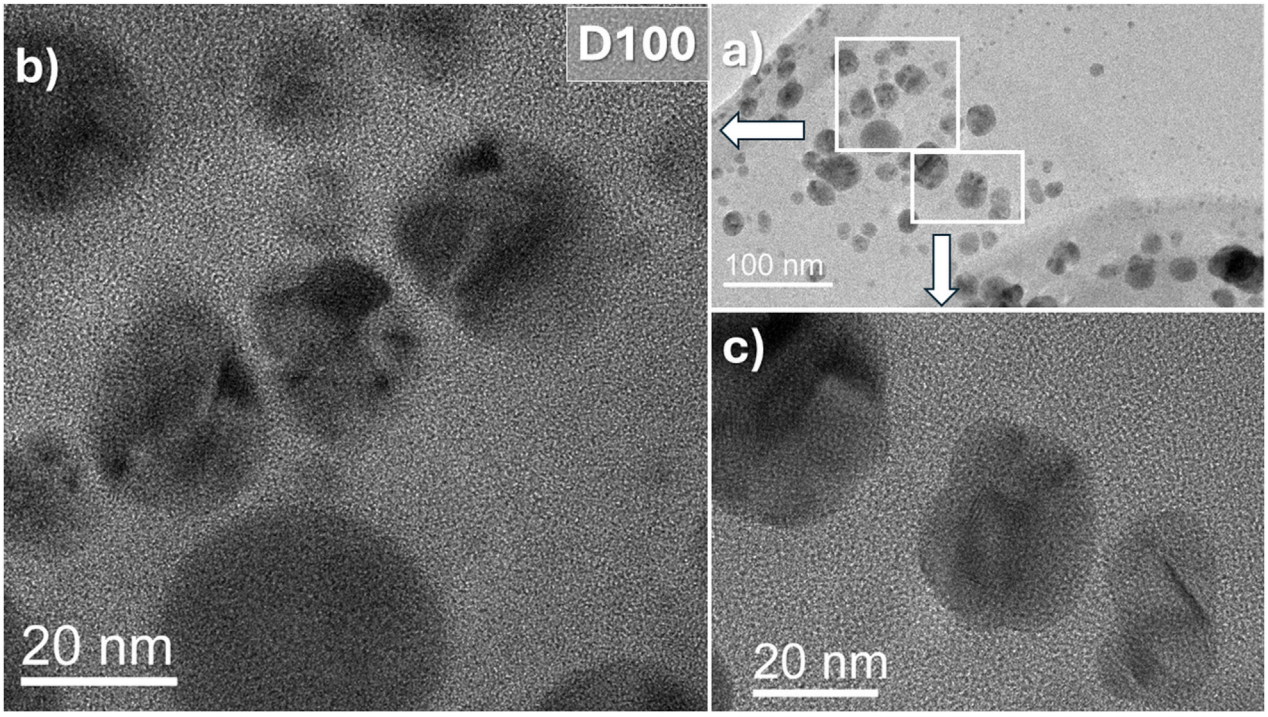

FIGURE 4
High-resolution transmission electron microscopy (HRTEM) of AgNPs synthesized with 100 mM of D-histidine. **(A)** Low magnification image of AgNPs in a grid area. **(B)** and **(C)** Zoom of the corresponding area as indicated in the boxes.

expressed as the tension in the photomultiplier of CD equipment. The tension in the photomultiplier results from the light absorption and scattering.

The AgNPs were analyzed by HRTEM (Figures 4, 5). Figure 4A shows many AgNPs synthesized with 100 mM of D-histidine in an extensive analysis area. Some of these AgNPs can be better visualized in Figures 5B,C, corresponding to two zooms of the respective white boxes. Figures 5A–F), shows HRTEM images of AgNPs synthesized with 100 mM of L-histidine. The images show the AgNPs with contours suggesting a corona formed by histidine molecules associated with the nanoparticles. Figure 5G) shows a pictorial representation of one AgNP associated with L-histidine molecules. Corona was not evidenced in AgNPs synthesized with 50 and 100 mM of D- and L-histidine and 50 mM of L-histidine.

More representative HRTEM images and the histograms of AgNPs produced with 50 and 100 mM of D- and L-histidine and the selection area electron diffraction (SAED) patterns are shown in the (Supplementary Figures S2–S5). The sizes were obtained from low-magnification TEM images to create a diameter distribution histogram. The Supplementary Material also shows the indexing for the distances between atomic planes obtained for AgNPs (Supplementary Figure S6). Consistently with CD spectra obtained for the enantiomeric pairs of chiral AgNPs, the SAED analysis shows that the AgNPs templated by D- and L-histidine constitute heterogeneous populations in which enantiomeric pairs of nanocrystals are formed mixed with other distorted nanocrystals without a correspondent pair in the sample obtained with the histidine isomer. The AgNPs were also characterized by dynamic light scattering and zeta potential (Figures 6A,B; Table 1).

Figure 6A shows the autocorrelation functions and the cumulant fits determined for AgNPs colloidal suspensions prepared with 50 and 100 mM of D- and L-histidine. Figure 6B shows the respective distributions of R_h as indicated in the Figure. The values of R_h were compared with the mean size of AgNPs obtained from the histograms presented in the (Supplementary Figures S2–S5). The discrepancy of R_h and mean size values, except for AgNPs prepared with 50 mM of L-histidine, indicated the formation of nanoparticle aggregates in the colloidal suspensions. The polydispersity indexes (PDI) are consistent with the mean size distribution of the AgNPs. The AgNPs produced with 50 and 100 mM of D- and L-histidine present positive zeta potential values that result from the contribution of histidine amino groups and imidazole lateral chain, as well as the reminiscent CTAB molecules that could remain associated with the nanoparticles. The quantification and R_h distributions of AgNPs (Table 1) are also consistent with similar characteristics in size and concentration obtained with 100 mM of the histidine isomers. Thus, the AgNPs obtained with 100 mM of D- and L-histidine were chosen for application in enzymatic catalysis.

3.1 Application of AgNPs

AgNPs produced with 100 mM of histidine were functionalized with the serine-protease POP, and the enzymatic activity was determined using a fluorescent substrate (Figure 7).

Figure 7B shows that the proteolytic activity of POP was twofold higher when associated with AgNPs produced with 100 mM of

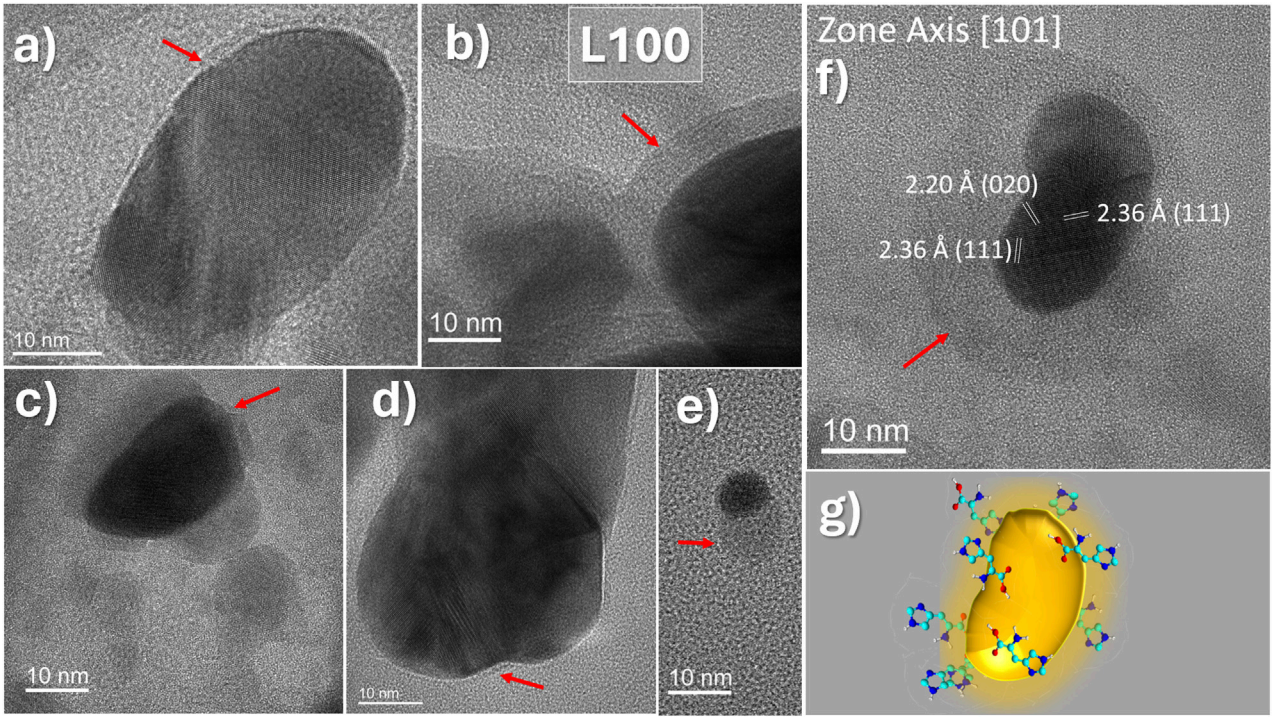

FIGURE 5
High-resolution transmission electron microscopy (HRTEM) of AgNPs synthesized with 100 mM of L-histidine (L100). **(A–F)** Panels show representative images of AgNPs in which the presence of a corona (red arrows) assigned to bound histidine is visible. In **(F)**, atomic plane distances are indexed for an AgNP oriented in [101] zone axis. **(G)** Pictorial representation of an AgNP capped by histidine molecules.

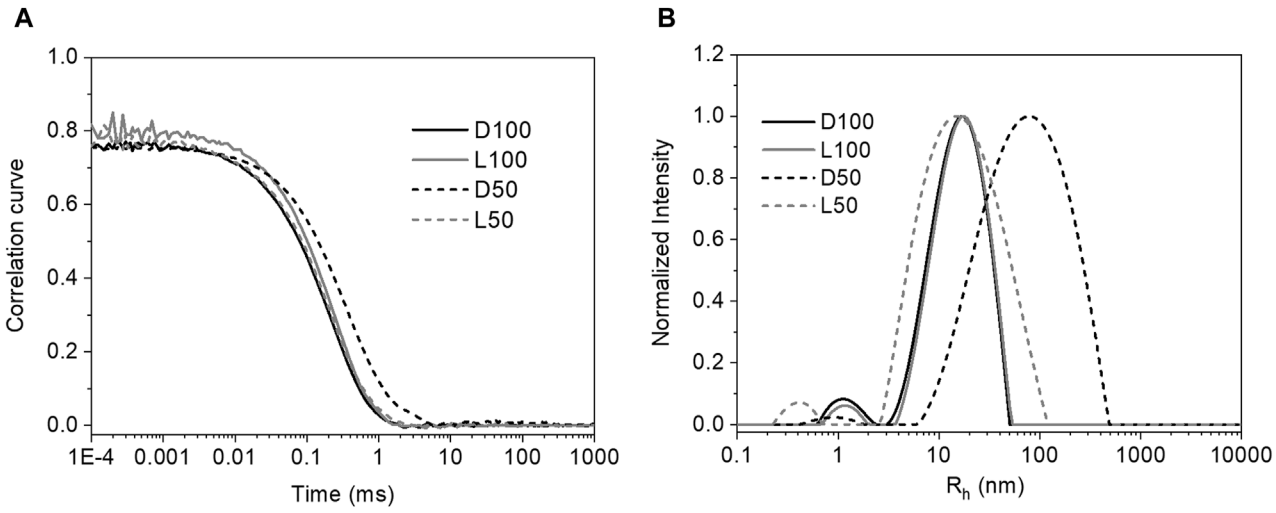

FIGURE 6
(A) Autocorrelation functions measured at 25°C for the AgNPs; **(B)** The respective distributions of R_h determined by the REPES algorithm.

D-histidine compared to the association with AgNPs produced with 100 mM of L-histidine. The differences in POP activities associated with D- and L-AgNPs are assigned to POP's more efficient substitution of D-histidine than L-histidine (Figure 7C). The functionalization of AgNPs was made using an enzymatic solution that presented activity 15 times higher when compared with that obtained with AgNPs produced with D-histidine. This result indicated that a large excess of enzyme relative to the AgNP concentration was removed from the suspension after the washing. The availability of AgNPs in the solution for the enzyme binding

TABLE 1 Parameters of AgNPs obtained by dynamic light scattering and electrophoretic mobility.

Sample (mM)	[AgNPs] (μg/mL)*	R_H (nm)	Mean size (nm)**	PDI	ζ (mV)	λ_{max} (nm)
AgNP L-His50	6.58	32.84	30 ± 12	0.45	+51.9	414.07
AgNP D-His50	4.17	59.98	9.5 ± 3	0.47	+67.0	410.92
AgNP L-His100	5.93	35.66	17 ± 9	0.38	+46.0	413.02
AgNP D-His100	5.73	31.67	19 ± 8	0.43	+66.5	412.98

*Determined by SPR, bands (Paramelle et al., 2014) and **From histograms (Supplementary Figures S2–S5).

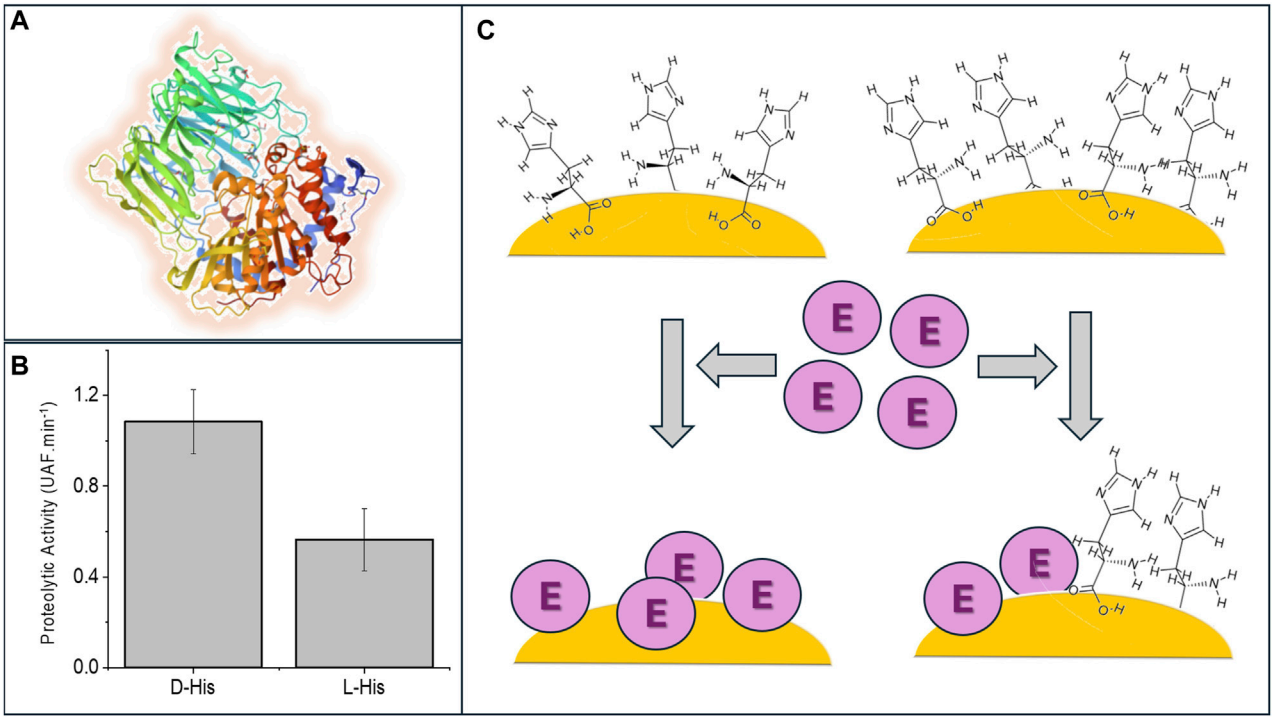

FIGURE 7
The association with chiral AgNPs influences the proteolytic activity of POP. **(A)** Cartoon representation of the tertiary structure of porcine POP from PDB 1QFM. **(B)** Comparative proteolytic activity of POP associated with AgNPs produced with 100 M of D- and L-histidine as indicated in the panel. **(C)** Schematic representations of the replacement of D- and L-histidine by POP on the surface of AgNPs that putatively are responsible for differences in POP activities. In the scheme, D-histidine (upper left side) was more efficiently displaced by POP from the AgNP surface than L-histidine (upper right side).

limited the enzymatic activity. The enzyme was expressed with His-tag, and the AgNP functionalization requires the displacing of histidine molecules of the nanoparticle corona. The specific influence of the chiral nanocrystal surface on the enzyme structure and activity could not be discarded. However, the more probable cause for the significant difference in the proteolytic activity would be the capacity of His-tag formed by L-histidine residues to compete with histidine molecules on the AgNP surface. In this regard, broad coronas were detected only in the HRTEM images of L-AgNPs (Figures 5A–F), suggesting a higher affinity of the L isomer for the AgNP surface. Therefore, the observed enantioselectivity in the D- and L-histidine corona could potentially distinguish the binding of POP to the nanocrystal. This result is consistent with a study by Kapon et al. (2021) showing evidence for new enantiospecific interaction force in chiral biomolecules. However, it is conceivable that such an amino acid/protein chemical exchange process might induce only marginal tertiary structural modifications and minor reversible structural alterations. It is noteworthy that characterizing these structural changes is challenging and may not entirely account for the differences observed in our activity assays.

Moreover, protein concentration poses challenges for utilizing spectroscopic techniques that are inherently insensitive to quantification. An alternative approach involves employing activity-site titration inhibitors. Nevertheless, it is essential to acknowledge that POP lacks a well-described inhibitor to facilitate tight-binding enzyme kinetic assays. Despite these challenges, we assumed that the constant affinity of prolyl oligopeptidase and its substrate remains unchanged after interaction with the nanocrystal, consistent in both D- and L-nanocrystal structures. This study will be continued by

screening the binding affinity of a diversity of his-tagged enzymes on chiral AgNPs.

4 Conclusion

D- and L-histidine can be used as templates and stabilizing agents for growing AgNPs on seeds of the same metal. Considering the chiral distorted AgNPs were grown on achiral Ag seeds, the affinity of histidine by the Ag surface was important to allow D- and L-histidine to confine the Ag nanocrystal growing on the seeds with chiral distortion. The concentration of AgNPs produced with 50 mM of D-histidine was lower than that obtained with L-histidine, but the AgNP yield was similar using 100 mM of D-and L-histidine. The AgNPs produced in the four experimental conditions remained stable for 1 year, as evidenced by the analysis of SPR bands. The condition in which even minimal changes were observed in the SPR bands was the synthesis carried out using 100 mM of L-histidine. According to CD spectra and corroborated by SAED analysis, enantiomeric pairs of AgNPs and other distorted Ag nanocrystals that are not enantiomerically paired were produced. However, even the mixed distorted Ag nanocrystals constituted enantiomeric pairs by the capping with the D- and L-histidine. The chirality of AgNPs significantly affects the binding and activity of POP, probably influenced by the more efficient displacement of D-histidine from the surface of the nanoparticles by the enzyme his-tag formed by L-histidine. The use of his-tag to immobilize recombinant enzymes on nanostructured metallic materials is a significant innovation of the present study.

Data availability statement

The raw data supporting the conclusions of this article will be made available by the authors, without undue reservation.

Author contributions

CB: Data curation, Investigation, Methodology, Validation, Writing–original draft. VT: Data curation, Investigation, Methodology, Validation, Writing–review and editing. MR: Investigation, Methodology, Validation, Writing–original draft, Formal Analysis. VO: Formal Analysis, Methodology, Conceptualization, Resources, Writing–original draft. JA: Conceptualization, Formal Analysis, Methodology, Resources, Data curation, Software, Writing–review and editing. MI: Conceptualization, Data curation, Formal Analysis, Methodology, Resources, Writing–review and editing, Investigation, Supervision. IN: Conceptualization, Data curation, Formal Analysis, Supervision, Writing–review and editing, Funding acquisition, Project administration.

Funding

The author(s) declare that financial support was received for the research, authorship, and/or publication of this article. This research was supported by FAPESP grants 2017/02317-2, 2023/09167-7, FAPESP fellowships 2023/14132-8 (C.C.S.B.), 2023/10315-0, 2022/07342-3, CNPq grant 313111-9, 423165/2021, CAPES 88887.7114539/2022-0.

Conflict of interest

The authors declare that the research was conducted in the absence of any commercial or financial relationships that could be construed as a potential conflict of interest.

The author(s) declared that they were an editorial board member of Frontiers, at the time of submission. This had no impact on the peer review process and the final decision.

Publisher's note

Supplementary material

The Supplementary Material for this article can be found online at: https://www.frontiersin.org/articles/10.3389/fnano.2024.1392694/full#supplementary-material

References

Ahn, H. Y., Lee, H. E., Jin, K., and Nam, K. T. (2013). Extended gold nano-morphology diagram: synthesis of rhombic dodecahedra using CTAB and ascorbic acid. *J. Mater. Chem. C* 1, 6861–6868. doi:10.1039/c3tc31135j

Basak, S., Singh, I., Ferranco, A., Syed, J., and Kraatz, H. B. (2017). On the role of chirality in guiding the self-assembly of peptides. *Angew. Chem. - Int. Ed.* 56, 13288–13292. doi:10.1002/anie.201706162

Batista, C. C. S., Alessandro, J., Albuquerque, B. L., Pavlova, E., Step, P., and Giacomelli, F. C. (2021). Colloids and surfaces A: physicochemical and engineering aspects microfluidic-assisted synthesis of uniform polymer-stabilized silver colloids. *Colloids Surfaces A Physicochem. Eng. Aspects* 618, 126438. doi:10.1016/j.colsurfa.2021.126438

Brito, A. M. M., Oliveira, V., Icimoto, M. Y., and Nantes-Cardoso, I. L. (2021). Collagenase activity of bromelain immobilized at gold nanoparticle interfaces for therapeutic applications. *Pharmaceutics* 13, 1143. doi:10.3390/pharmaceutics13081143

Bronzato, J. D., Tofanello, A., Oliveira, M. T., Bettini, J., Brito, A. M. M., Costa, S. A., et al. (2022). Virucidal, photocatalytic and chiromagnetic cobalt oxide quantum dots. *Appl. Surf. Sci.* 576, 151847. doi:10.1016/j.apsusc.2021.151847

Cho, N. H., Guerrero-Martínez, A., Ma, J., Bals, S., Kotov, N. A., Liz-Marzán, L. M., et al. (2023). Bioinspired chiral inorganic nanomaterials. *Nat. Rev. Bioeng.* 1, 88–106. doi:10.1038/s44222-022-00014-4

Cornelissen, JJLM, Rowan, A. E., Nolte, R. J. M., and Sommerdijk, NAJM (2001). Chiral architectures from macromolecular building blocks. *Chem. Rev.* 101, 4039–4070. doi:10.1021/cr990126i

Đorđević, L., Arcudi, F., D'Urso, A., Cacioppo, M., Micali, N., Bürgi, T., et al. (2018). Design principles of chiral carbon nanodots help convey chirality from molecular to nanoscale level. *Nat. Commun.* 9, 3442. doi:10.1038/s41467-018-05561-2

Ferro, E. S., Gewehr, M. C. F., and Navon, A. (2020). Thimet oligopeptidase biochemical and biological significances: past, present, and future directions. *Biomolecules* 10 (10), 1229. doi:10.3390/BIOM10091229

Gao, R., Xu, X., Kumar, P., and Xu, C. (2022). Tapered chiral nanoparticles as broad-spectrum thermally stable antivirals for SARS-CoV-2 variants. *Proc. Natl. Acad. Sci.* 121 (13), e2310469121. doi:10.1073/pnas.2310469121

Ghosh, S., Bloom, B. P., Lu, Y., Lamont, D., and Waldeck, D. H. (2020). Increasing the efficiency of water splitting through spin polarization using cobalt oxide thin film catalysts. *J. Phys. Chem. C* 124, 22610–22618. doi:10.1021/acs.jpcc.0c07372

Gontijo, T. B., Lima, P. S., Icimoto, M. Y., Neves, R. L., de Alvarenga, É. C., Carmona, A. K., et al. (2021). Cathepsin K inhibitors based on 2-amino-1,3,4-oxadiazole derivatives. *Bioorg. Chem.* 109, 104662. doi:10.1016/j.bioorg.2021.104662

Halas, N. J., Lal, S., Chang, W. S., Link, S., and Nordlander, P. (2011). Plasmons in strongly coupled metallic nanostructures. *Chem. Rev.* 111, 3913–3961. doi:10.1021/cr200061k

Hannula, M. J., Myöhänen, T. T., Tenorio-Laranga, J., Männistö, P. T., and Garcia-Horsman, J. A. (2013). Prolyl oligopeptidase colocalizes with α-synuclein, β-amyloid, tau protein and astroglia in the post-mortem brain samples with Parkinson's and Alzheimer's diseases. *Neuroscience* 242, 140–150. doi:10.1016/j.neuroscience.2013.03.049

Hatano, M., Okamoto, H., Kawakami, T., Toh, K., Nakatsuji, H., Sakakura, A., et al. (2018). Enantioselective aza-Friedel-Crafts reaction of furan with α-ketimino esters induced by a conjugated double hydrogen bond network of chiral bis(phosphoric acid) catalysts. *Chem. Sci.* 9, 6361–6367. doi:10.1039/c8sc02290a

Houben, L., Weissman, H., Wolf, S. G., and Rybtchinski, B. (2020). A mechanism of ferritin crystallization revealed by cryo-STEM tomography. *Nature* 579, 540–543. doi:10.1038/s41586-020-2104-4

Icimoto, M. Y., Brito, A. M. M., Ramos, M. P. C., Oliveira, V., and Nantes-Cardoso, I. L. (2020). Increased stability of oligopeptidases immobilized on gold nanoparticles. *Catalysts* 10, 78. doi:10.3390/catal10010078

Jiang, S., Chekini, M., Qu, Z. B., Wang, Y., Yeltik, A., Liu, Y., et al. (2017). Chiral ceramic nanoparticles and peptide catalysis. *J. Am. Chem. Soc.* 139, 13701–13712. doi:10.1021/jacs.7b01445

Kaarniranta, K., Sinha, D., Blasiak, J., Kauppinen, A., Veréb, Z., Salminen, A., et al. (2013). Autophagy and heterophagy dysregulation leads to retinal pigment epithelium dysfunction and development of age-related macular degeneration. *Autophagy* 9, 973–984. doi:10.4161/AUTO.24546

Kapon, Y., Saha, A., Duanis-Assaf, T., Stuyver, T., Ziv, A., Metzger, T., et al. (2021). Evidence for new enantiospecific interaction force in chiral biomolecules. *Chem* 7, 2787–2799. doi:10.1016/j.chempr.2021.08.002

Kauppinen, A., Paterno, J. J., Blasiak, J., Salminen, A., and Kaarniranta, K. (2016). Inflammation and its role in age-related macular degeneration. *Cell Mol. Life Sci.* 73, 1765–1786. doi:10.1007/S00018-016-2147-8

Lambeir, A.-M. (2011). Interaction of prolyl oligopeptidase with α-Synuclein. *CNS Neurological Disord. - Drug Targets* 10, 349–354. doi:10.2174/187152711794653878

Liu, X., Du, Y., Wang, S., Huang, Y., Tian, Y., García-Lojo, D., et al. (2023). Histidine-Mediated synthesis of chiral cobalt oxide nanoparticles for enantiomeric discrimination and quantification. *Small* 19, e2205187. doi:10.1002/SMLL.202205187

Majee, R., Kumar, A., Das, T., Chakraborty, S., and Bhattacharyya, S. (2020). Tweaking nickel with minimal silver in a heterogeneous alloy of decahedral geometry to deliver platinum-like hydrogen evolution activity. *Angew. Chem. - Int. Ed.* 59, 2881–2889. doi:10.1002/anie.201913704

Malishev, R., Arad, E., Bhunia, S. K., Shaham-Niv, S., Kolusheva, S., Gazit, E., et al. (2018). Chiral modulation of amyloid beta fibrillation and cytotoxicity by enantiomeric carbon dots. *Chem. Commun.* 54, 7762–7765. doi:10.1039/C8CC03235A

Mun, J., Kim, M., Yang, Y., Badloe, T., Ni, J., Chen, Y., et al. (2020). Electromagnetic chirality: from fundamentals to nontraditional chiroptical phenomena. *Light Sci. Appl.* 9, 139. doi:10.1038/s41377-020-00367-8

Naaman, R., and Waldeck, D. H. (2015). Spintronics and chirality: spin selectivity in electron transport through chiral molecules. *Annu. Rev. Phys. Chem.* 66, 263–281. doi:10.1146/annurev-physchem-040214-121554

Naito, M., Iwahori, K., Miura, A., Yamane, M., and Yamashita, I. (2010). Circularly polarized luminescent CDs quantum dots prepared in a protein nanocage. *Angew. Chem. - Int. Ed.* 49, 7006–7009. doi:10.1002/anie.201002552

Nantes-Cardoso, I. L., and Tofanello de Souza, A. (2019). *Processo de síntese verde simultânea de nanopartículas metálicas E magnéticas com USO de proteínas armazenadoras de ferro fundação universidade federal do abc—ufabc (br/sp) iseli lourenço nantes-cardoso; aryane tofanello de souza*. Rio de Janeiro, Brazil: Instituto Nacional de Propriedade Intelectual (INPI), 1–23.

Neves, R. L., Marem, A., Carmona, B., Arata, J. G., Cyrillo Ramos, M. P., Justo, G. Z., et al. (2023). Expression of thimet oligopeptidase (THOP) modulated by oxidative stress in human multidrug resistant (MDR) leukemia cells. *Biochimie* 212, 21–30. doi:10.1016/j.biochi.2023.03.013

Norrbacka, S., Lindholm, D., and Myöhänen, T. T. (2019). Prolyl oligopeptidase inhibition reduces PolyQ aggregation and improves cell viability in cellular model of Huntington's disease. *J. Cell. Mol. Med.* 23, 8511–8515. doi:10.1111/jcmm.14675

Oh, S. H., Hong, M. H., Shin, H., Amornkitbamrung, U., In, Y., Wang, Z., et al. (2022). C-axis-oriented platelets of crystalline hydroxyapatite in biomimetic intrafibrillar mineralization of polydopamine-functionalized collagen type I. *ACS Omega* 7, 4821–4831. doi:10.1021/acsomega.1c05198

Oh, Y., Lai, J. S. Y., Min, S., Huang, H. W., Liberles, S. D., Ryoo, H. D., et al. (2021). Periphery signals generated by Piezo-mediated stomach stretch and Neuromedin-mediated glucose load regulate the Drosophila brain nutrient sensor. *Neuron* 109, 1979–1995.e6. doi:10.1016/J.NEURON.2021.04.028

Paramelle, D., Sadovoy, A., Gorelik, S., Free, P., Hobley, J., and Fernig, D. G. (2014). A rapid method to estimate the concentration of citrate capped silver nanoparticles from UV-visible light spectra. *Analyst* 139, 4855–4861. doi:10.1039/c4an00978a

Peng, Y., Yao, Y., Li, L., Wu, Z., Wang, S., and Luo, J. (2018). White-light emission in a chiral one-dimensional organic-inorganic hybrid perovskite. *J. Mater. Chem. C* 6, 6033–6037. doi:10.1039/c8tc01150h

Polgár, L. (2002). The prolyl oligopeptidase family. *Cell. Mol. Life Sci.* 59, 349–362. doi:10.1007/s00018-002-8427-5

Prohaska, R., and Salzer, U. (2018). "Flotillin-2 (FLOT2)," in *Encyclopedia of signaling molecules* (Cham: Springer International Publishing), 1778–1786. doi:10.1007/978-3-319-67199-4_646

Qiu, M., Zhang, L., Tang, Z., Jin, W., Qiu, C. W., and Lei, D. Y. (2018). 3D metaphotonic nanostructures with intrinsic chirality. *Adv. Funct. Mater* 28, 1803147. doi:10.1002/adfm.201803147

Rea, D., and Fulop, V. (2011). Prolyl oligopeptidase structure and dynamics. *CNS Neurological Disord. - Drug Targets* 10, 306–310. doi:10.2174/187152711794653850

Santos, G. S., Oyadomari, W. Y., Carvalho, E. A., Torquato, R. S., and Oliveira, V. (2020). Prolyl endopeptidase-like facilitates the α-synuclein aggregation seeding, and this effect is reverted by serine peptidase inhibitor pmsf. *Biomolecules* 10, 962. doi:10.3390/biom10060962

Suzuki, N., Wang, Y., Elvati, P., Qu, Z. B., Kim, K., Jiang, S., et al. (2016). Chiral graphene quantum dots. *ACS Nano* 10, 1744–1755. doi:10.1021/acsnano.5b06369

Tang, Y., and Cohen, A. E. (2011). Enhanced enantioselectivity in excitation of chiral molecules by superchiral light. *Science* 332 (332), 333–336. doi:10.1126/science.1202817

Tofanello, A., Bronzato, J. D., Rettori, C., Nascimento, O. R., and Nantes-Cardoso, I. L. (2021). Conversion of ferritin ferrihydrite core to magnetite by gold ions binding and the derived nanoparticle formation. *J. Nanostructure Chem.* 12, 401–416. doi:10.1007/s40097-021-00423-8

Toppila, M., Hytti, M., Korhonen, E., Ranta-aho, S., Harju, N., Forsberg, M. M., et al. (2023). The prolyl oligopeptidase inhibitor KYP-2047 is cytoprotective and anti-inflammatory in human retinal pigment epithelial cells with defective proteasomal clearance. *Antioxidants* 12 (12), 1279. doi:10.3390/ANTIOX12061279

Wen, Y., He, M.-Q., Yu, Y.-L., and Wang, J.-H. (2021). Biomolecule-mediated chiral nanostructures: a review of chiral mechanism and application. *Adv. Colloid Interface Sci.* 289, 102376. doi:10.1016/j.cis.2021.102376

Xiao, L., An, T., Wang, L., Xu, X., and Sun, H. (2020a). Novel properties and applications of chiral inorganic nanostructures. *Nano Today* 30, 100824. doi:10.1016/j.nantod.2019.100824

Xiao, L., An, T., Wang, L., Xu, X., and Sun, H. (2020b). Novel properties and applications of chiral inorganic nanostructures. *Nano Today* 30, 100824. doi:10.1016/j.nantod.2019.100824

Xu, L., Wang, X., Wang, W., Sun, M., Choi, W. J., Kim, J. Y., et al. (2022). Enantiomer-dependent immunological response to chiral nanoparticles. *Nature* 601, 366–373. doi:10.1038/s41586-021-04243-2

Yeom, J., Santos, U. S., Chekini, M., Cha, M., de Moura, A. F., and Kotov, N. A. (2018). Chiromagnetic nanoparticles and gels. *Science* 359, 309–314. doi:10.1126/science.aao7172

Yuan, C., Li, X., Semin, S., Feng, Y., Rasing, T., and Xu, J. (2018). Chiral lead halide perovskite nanowires for second-order nonlinear optics. *Nano Lett.* 18, 5411–5417. doi:10.1021/acs.nanolett.8b01616

Zhao, X., Zang, S.-Q., and Chen, X. (2020). Stereospecific interactions between chiral inorganic nanomaterials and biological systems. *Chem. Soc. Rev.* 49, 2481–2503. doi:10.1039/d0cs00093k